



CHORUS

This is the accepted manuscript made available via CHORUS. The article has been published as:

Excitation functions of heavy residues produced in the $^{14}\text{N} + ^{103}\text{Rh}$ reaction up to 400 MeV: Analysis of the pre-equilibrium mechanism with the hybrid Monte Carlo simulation model

J. Acharya, S. Mukherjee, G. F. Steyn, N. L. Singh, and A. Chatterjee

Phys. Rev. C **93**, 024608 — Published 12 February 2016

DOI: [10.1103/PhysRevC.93.024608](https://doi.org/10.1103/PhysRevC.93.024608)

Excitation functions of heavy residues produced in the $^{14}\text{N}+^{103}\text{Rh}$ reaction up to 400 MeV: Analysis of the pre-equilibrium mechanism with the Hybrid Monte Carlo Simulation (HMS) model

J. Acharya¹, S. Mukherjee^{1*}, G.F. Steyn², N.L. Singh¹, A. Chatterjee¹

¹ *Physics Department, Faculty of Science, M.S. University of Baroda, Vadodara-390002, India*

² *iThemba LABS, P.O. Box 722, Somerset West, 7129, South Africa*

* *Corresponding Author: sk.mukherjee-phy@msubaroda.ac.in*

The excitation functions of heavy residues, produced in the interaction of ^{14}N with ^{103}Rh , have been measured over the projectile energy region from threshold up to 400 MeV by means of the activation method in conjunction with γ -ray spectroscopy. Cross sections for fifteen reaction residues are presented, namely ^{104}Cd , $^{103,104,105}\text{Ag}$, $^{99,100,101}\text{Pd}$, $^{97,99,101}\text{Rh}$, $^{95,97}\text{Ru}$ and $^{94,95,96}\text{Tc}$. The experimental data are compared with theoretical model predictions using the Hybrid Monte Carlo Simulation (HMS) model as implemented in the recently released ALICE 2014 code. The theory assumes that the dominant pre-equilibrium mechanism includes multi-nucleon and cluster emission in the initial stages of the interaction between the projectile and the target nucleus. Overall, the theoretical predictions provide a satisfactory agreement with the trend of the present experimental results for most of the observed reaction residues. This provides strong evidence that the underlying reaction mechanisms in the code are appropriately described. Overall, the Obninsk level densities give the best results in the present study.

I. INTRODUCTION

In heavy-ion reactions, a complex series of processes can occur due to the relatively large number of nucleons involved as well as a large amount of angular momentum that a projectile can transfer to the target nucleus. These processes include the formation of an excited intermediate nucleus in a state far from statistical equilibrium, its equilibration by means of intra-nuclear interactions, pre-equilibrium emission of nucleons and light clusters and finally the formation of an intermediate equilibrated nucleus, which further evaporates particles and also emits γ -rays and/or fissions [1–4]. There is a

statistical competition between these different reaction mechanisms, which all contribute to the cross sections for the formation of specific heavy residues. It has been known for many years that the small but measurable cross sections for the formation of some of the heavy residues cannot be accounted for by considering only evaporation of particles from an equilibrated compound nucleus. Even at incident energies barely higher than the Coulomb barrier, pre-equilibrium emission of nucleons during the thermalization of the composite nucleus has to be taken into consideration in order to reproduce the formation cross sections of the heavy (target-like) residues [5].

In recent years, a significant body of experimental data on excitation functions, forward recoil ranges and angular distributions of residues has been accumulated at incident energies up to 400 MeV [2,3, 6–8] in the mass region similar to the present work. This allowed a comprehensive analysis of all the processes which take place, both in the initial projectile-target interaction and during the de-excitation of the non-equilibrated hot nuclei which are produced in the interaction. The analysis of these data have suggested that in addition to the contributions from projectile fragmentation, deep inelastic collisions or other non-fusion processes, a significant amount of pre-equilibrium particles are also emitted. The possible importance of pre-equilibrium decay in heavy-ion reactions has been earlier discussed by Blann [9,10]. Furthermore, a large fraction of α -particles which initially participated in the incomplete fusion processes are emitted in the pre-equilibrium stage as well.

The yields of residues formed by α -particle emission should differ appreciably for the respective contributing reaction mechanisms, which depend sensitively on the incident projectile energy. There exists experimental evidence of pre-equilibrium nucleon and α -emission that contributes significantly to the subsequent de-excitation following the fusion of heavy ions [11,12]. In nuclear reactions at intermediate energies, a wide variety of residues are produced. The yields, energy spectra and angular distributions are valuable information for applications and inter-disciplinary fields [13]. The development of phenomenological theories is important in the physics of such reaction data. Earlier, basic reaction models such as the exciton model [14] and Geometry-Dependent Hybrid Model (GDH) [11,15] were being employed for analyzing these data, in particular for their description of pre-equilibrium reactions. However, a comparison of measurements

with model predictions often showed limited success, especially for reactions induced by heavy ions.

Gadioli et al. [1–3] presented excitation function data as well as energy spectra and angular distributions of α -particles and intermediate mass fragments (IMFs) for $^{12}\text{C}+^{103}\text{Rh}$ and $^{16}\text{O}+^{103}\text{Rh}$ systems, from the Coulomb barrier up to 400 MeV. In order to understand these data, complete fusion and break-up-fusion processes were assumed to depend on the mean-field interaction between the target and projectile nuclei. The evolution of the system towards equilibrium was studied by following the nucleon-nucleon cascade, solving a set of Boltzmann Master Equations (BME). The model was successful in arriving at a generally good agreement between the measured data and theoretical predictions.

Recently, a new version of the code ALICE [11–13,16–18], namely ALICE 2014, has become available, providing a theoretical framework for calculating cross sections for the production of residues at intermediate energies. The new code incorporates the Hybrid Monte Carlo Simulation (HMS) model for calculating cross sections for pre-equilibrium reactions induced by light and heavy ions. It includes multiple pre-equilibrium emission processes as well as a semi-classical treatment of angular momentum transfer effects. Considering the wide use of the HMS model in applications, and to ensure its predictive power, it is important to confront the code to a wide variety of reactions, especially for reactions induced by different medium-mass and heavy ions.

In this work, excitation functions for the formation of residues in the interaction of ^{14}N projectiles with ^{103}Rh target nuclei were measured from the Coulomb barrier up to 400 MeV. The experiment presented here was designed to establish the extent to which pre-equilibrium emission of α -particles is present in heavy-ion reactions leading to the heavy fusion-like/target-like residues. The use of ^{14}N projectiles enhances the data set for comparisons as data for ^{12}C and ^{16}O -induced reactions have already been measured on this nucleus [1-3]. It provides a valuable testing ground for the HMS model. In particular, it may be interesting to look for differences in the α -particle and IMF emission spectra, as well as the heavy residues left behind, from the interactions of a projectile that is not a pure α -like nucleus like ^{12}C and ^{16}O . Here we present the excitation functions for heavy

reaction residues and a separate investigation on the emission spectra of light clusters is in progress. Also, the present experimental data, measured with high precision, is a useful addition to the global nuclear database in this mass region.

II. EXPERIMENTAL PROCEDURE

In the present investigation, excitation functions for fifteen reaction residues were obtained, namely ^{104}Cd , $^{103,104,105}\text{Ag}$, $^{99,100,101}\text{Pd}$, $^{97,99,101}\text{Rh}$, $^{95,97}\text{Ru}$ and $^{94,95,96}\text{Tc}$ for the system $^{14}\text{N}+^{103}\text{Rh}$ up to 400 MeV, using the activation technique in conjunction with off-line γ -ray spectroscopy. The separated sector cyclotron (SSC) of iThemba LABS, capable of accelerating ^{14}N ions up to several tens of MeV/nucleon, provided the ^{14}N beam with an incident energy of nominally 400 MeV. The beam formation started with an external cyclotron resonance (ECR) ion source, followed by injection into a solid pole cyclotron (SPC2) which is an injector cyclotron for further acceleration. The SSC provided the final acceleration to the desired beam energy.

The beam current intercepted by the target and beam stop was measured with a Brookhaven Instruments model 1000C current integrator. The accumulated charge was also logged in 10 second intervals by means of the data acquisition system XSYS. In this way the beam intensity fluctuations during bombardments were monitored. This was done because beam fluctuations may yield inaccuracies in the results, especially in the case of radionuclides with half-lives shorter than or of the same order of magnitude as the bombardment time, if not properly corrected for.

A metallic Rh foil stack was prepared for bombardment with a ^{14}N beam. Self-supporting foils of 99.99% purity were supplied by Goodfellow Ltd. (Cambridge, UK). The stack consisted of a single 5 μm thick Ti monitor foil, followed by several Rh foils with a nominal thickness of 32.02 mg/cm^2 . The thickness of the stack was such that it stopped the beam. It was irradiated for 5 hours at an incident energy of 395.1 MeV and an average beam current of 50 nA. After wards, an autoradiogram of the Ti foil confirmed that the focus of the beam remained on the center of the stack for the entire

duration of the bombardment. The beam energy was determined by means of a calibrated 90° analysis magnet with an uncertainty of less than 1 MeV.

The collected γ -ray spectra were analysed by means of the EMCAPLUS version 2.01 spectrum analysis software provided by Silena, in combination with the spreadsheet program Excel. The EMCAPLUS software was used for photopeak searches, area and statistical error calculations, background subtraction and, in a few cases, multiple deconvolution where the photopeaks overlapped. The data sorting program EVAL of the data acquisition system XSYS was used to extract the current integrator and timer scalar values from the event file logged during the experimental bombardment. The radionuclides produced in the ^{103}Rh target foils were identified by means of their characteristic x- and/or γ -lines. The decay data used in the analysis were taken from the literature [19].

III. DATA ANALYSIS

A. Experimental cross sections

The experimental production cross sections were obtained from the photopeak area extracted from the measured photon spectra by means of the following expressions:

$$\sigma(\text{mb}) = \frac{A_p T_1 K}{\tau \epsilon_\gamma \epsilon_e I_t N_0 \exp(-\lambda(T_m - T_1)) [1 - \exp(-\lambda T_1)] (1 \times 10^{-27})},$$

where A_p is the photopeak area of a particular x-ray or γ -ray line, $t = T_1$ is the duration of the bombardment where $t = 0$ is taken as the start time of bombardment, K is a correction factor for beam intensity fluctuations, τ is the live counting time, ϵ_γ is the branching ratio (intensity) of the photon line, ϵ_e is the efficiency of the detector, I_t is the total number of beam particles accumulated on the target during bombardment, N_0 is the total number of target nuclei per unit area (cm^{-2}), λ is the decay constant of the particular radionuclide, and T_m is the mean value of the measuring counting interval. All times have units of seconds and the result of the above equation is given in units of millibarn (mb). The factor K is given by

$$K = \frac{\left(\sum_{i=1}^n \Delta I_i \right) [\exp(\lambda T_1) - 1]}{\lambda T_1 \sum_{i=1}^n \Delta I_i \exp(\lambda h_i)},$$

where n is the number of current integrator readings logged during the bombardment period (scalar values were logged every 10 s), ΔI_i is the beam current integrated (or the number of beam particles on target) during the i^{th} time increment (of 10 s duration) during the bombardment, $1 \leq i \leq n$, and $t = h_i$ is the end of each time increment since the start of the bombardment. Finally, the mean-value time of counting is given by

$$T_m = -\frac{1}{\lambda} \ln \left[\frac{\exp[-\lambda(T_3 - T_2)]}{-\lambda(T_3 - T_2)} \right],$$

where $t = T_2$ denotes the start time of the counting period and $t = T_3$ denotes the end time of the counting period, relative to $t = 0$ being the start time of the bombardment.

The factor K may become important whenever the half-life of a particular radionuclide is shorter than or of the same order of magnitude as the bombardment time. In such cases, K can be strongly dependent on fluctuations in the beam intensity and become different from a normative value of unity.

B. Detector calibration

Both energy and efficiency calibrations were performed using standard sources of ^{133}Ba and ^{152}Eu , traceable to the BIPM. The ^{133}Ba source has a number of strong characteristic x -ray lines at 30.6 keV (34.4%), 31.0 keV (63.5%) and 35.0 keV (18.8%), which were useful for the calibration of the APTEC planar HPGe x -ray detector. The ^{152}Eu has strong γ -lines over the entire energy region from 121 keV to 1408 keV. Although the energy response of both the APTEC x -ray and EG&G ORTEC coaxial HPGe γ -ray detectors were very nearly linear, third-order polynomial fits were used for the energy calibration.

C. Uncertainty analysis

The uncertainty values of the experimental cross sections were estimated by summing all the contributing uncertainties in quadrature, and were typically between 15% and 20%. This includes the counting statistics, beam loss as a result of non-elastic nuclear interactions (2%), target thickness (10%), accumulated beam charge (2%), detector efficiency (5%), counting geometry (5%), photopeak integration (2%), and branching ratios (2%).

IV. THEORETICAL CALCULATIONS

Theoretical calculations were performed using the recently released computer code ALICE 2014 [11–13, 16–18]. This nuclear reaction code is the latest version of the so-called HMS-ALICE codes, in which pre-equilibrium emission of both nucleons and light clusters is based on the Hybrid Monte Carlo Simulation (HMS) model [17]. All cascades are terminated in the Weisskopf-Ewing evaporation model [20] and the equilibrium emission of both nucleons and light clusters can be selected. The options for emission were taken to be similar, i.e. both pre-equilibrium as well as equilibrium emission of n , p , ${}^2\text{H}$, ${}^3\text{H}$, ${}^3\text{He}$, ${}^4\text{He}$ were chosen for the present calculations. Calculations were made with three forms of the nuclear level density: Kataria-Ramamurthy (KR) [21], Obninsk [22] (OB), and back-shifted Fermi gas (FG). The OB and KR forms do not have any adjustable parameters. For FG we made the calculations with $'a' = A/9$, which is the default value. The changes resulting in varying $'a'$ in the range of $A/7$ to $A/11$ MeV^{-1} is 10% or less throughout the energy region and this is shown in Fig 7. The ALICE 2014 code contains an error in the calculation of KR level densities which we have corrected. The other input parameters were set to the default values of the code. Further details of the code are available in the literature [11-16].

V. RESULTS AND DISCUSSION

The experimental cross sections are presented in Table I and are compared with the ALICE 2014 theoretical predictions in Figs. 1–6. The calculated excitation functions are

shown as dashed curves (using Obninsk level densities), solid curves (using Fermi gas level densities) and dash-dot curves (using Kataria-Ramamurthy level densities). In the case of cumulative cross sections for the formation of the observed residues, the fractional contributions from precursor decay were summed to the directly produced contribution. These fractional precursor contributions were obtained by adopting the procedure given in the literature [1,2].

The silver residues observed in this work are $^{103,104,105}\text{Ag}$, shown in Fig. 1. The experimental excitation function of ^{103}Ag exhibits a broad peak with a maximum of ~ 145 mb at 250.9 MeV, beyond which the slope of the curve decreases monotonically toward higher energies. The excitation functions of ^{104}Ag and ^{105}Ag show similar trends, reaching maxima of ~ 146 mb and ~ 389 mb at 176.8 MeV, respectively. The theoretical predictions with all three level-density formalisms (OB, FG and KR) are reasonable in the case of ^{103}Ag isotope. In the case of $^{104,105}\text{Ag}$ both FG and KR gives a better agreement than OB level density, above 250 MeV. Amore pronounced under prediction is consistently observed with the all the three level densities below 250 MeV. However, the discrepancy is more pronounced in the case of FG and KR as compared to OB level density for $^{104,105}\text{Ag}$ isotopes.

The only residue of cadmium observed in this work is ^{104}Cd , shown in Fig. 2. Here the calculations with all the three level-density formalisms show nearly identical results, which are quite close to the data. The excitation function is rather structure less and almost constant between 200 and 300 MeV. The measurements seem to support the three local maxima predicted by the calculations but shifted towards higher energies. The experimental maximum is 137 mb at 215.8 MeV. Both the FG and OB level densities gives similar results in the entire energy region, while KR level density underestimates the experimental results below 150 MeV.

The observed palladium residues are $^{99,100,101}\text{Pd}$, shown in Fig. 3. The shapes of these excitation functions are also quite structure less, rising rather gently from their respective thresholds to exhibit very broad peak. Beyond the peak maxima, the decreasing trend of the excitation functions is quite small, thus their appearance seems almost flat towards higher energies. The calculations show a marked under prediction towards lower energies

in the cases of ^{100}Pd and ^{101}Pd . This discrepancy is not observed in the case of ^{99}Pd , however, an over-prediction is evident towards higher energies for both OB and FG level densities. The overall agreement with the measurements is markedly better when using the OB level density, in comparison with those given by FG and KR.

The excitation functions for the $^{97,99,101}\text{Rh}$, $^{95,97}\text{Ru}$ and $^{94,95,96}\text{Tc}$ residues exhibit very similar trends, as shown in Figs. 4–6. No prominent peaks or local maxima are observed. Rather, the excitation functions rise from their respective thresholds up to nearly constant plateaus towards higher energies. The theoretical calculations reproduce the plateaus very satisfactorily when the OB level densities are used. In contrast, rather serious under-predictions are evident in some of the cases, that is, Rh, Ru and Tc isotopes where FG and KR level density options are used. Overall in the above mentioned three sets of isotopes, OB gives by far the best agreement in comparison to the FG and KR options of level density.

Figs. 8-10 show the comparison of three of the presently measured excitation functions ($^{14}\text{N}+^{103}\text{Rh}$) with those measured earlier for the systems ^{12}C , $^{16}\text{O} + ^{103}\text{Rh}$ up to 400 MeV [1-3]. Same global parameters were used in the HMS model calculations in all the three systems. Three typical excitation functions for the residues, ^{94}Tc , ^{99}Rh and ^{100}Pd were selected for inter comparison of the systems with the present HMS model calculations. In Fig. 8, it may be observed that excitation function for the ^{94}Tc gives the best results for OB level density for $^{12}\text{C}+^{103}\text{Rh}$ system between 200 to 400 MeV, while for $^{14}\text{N}+^{103}\text{Rh}$ the results are better with OB level densities between 250 to 400 MeV. In the case of $^{16}\text{O}+^{103}\text{Rh}$, there is a gross underestimation by all the three level densities. In case of excitation function of ^{99}Rh (Fig. 9), both ^{12}C , $^{14}\text{N}+^{103}\text{Rh}$ systems gives similar and best results with OB level density, while for $^{16}\text{O}+^{103}\text{Rh}$ system the calculations underestimates the experimental results. In Fig. 10, $^{12}\text{C}+^{103}\text{Rh}$ gives the best agreement with all the three level densities (OB, KR and FG) as compared to the ^{14}N , $^{16}\text{O}+^{103}\text{Rh}$. In general, it may be concluded that the present theoretical and experimental results are quite close in agreement with the $^{12}\text{C}+^{103}\text{Rh}$ system, while for the $^{16}\text{O}+^{103}\text{Rh}$ the theoretical results significantly underestimate the experimental results.

A. Level Density Analysis

The absolute values of level density are vastly different. This is illustrated in Fig. 11 for one case. It will be noticed that at 200 MeV excitation, the OB level density is 20 orders of magnitude less than the FG level density with $a = A/7 \text{ MeV}^{-1}$, however, it is the excitation energy dependence that matters and not the absolute value of level density. As seen in the figure, OB level density has a distinctly different energy dependence as compared to other level density forms. It is important to note that in the original formulation of the KR level density [21] excitation energies above 60 MeV were not considered. For higher excitation the FG ($a = A/9 \text{ MeV}^{-1}$) level density form scaled to the 60 MeV KR value is used in ALICE 2014. The OB level density was formulated relatively recently as compared to FG and KR and it is heartening to note that overall it performs better in comparison to the present data. It is true that specific cases show differing degrees of agreement in different energy ranges, however this is only to be expected for calculations of a global nature without adjustable parameters.

As already mentioned earlier, varying the value of the FG level density parameter between $A/7$ and $A/11 \text{ MeV}^{-1}$ only results in small changes. As an example of this insensitivity, Fig. 7 shows calculations using $a = A/7$, $A/9$ and $A/11$ for the excitation function of the ^{100}Pd residue. Consequently, a value of $A/9$ was adopted throughout for the remainder of the calculations.

VI. SUMMARY AND CONCLUSIONS

Excitation functions for fifteen reaction residues were measured in the $^{14}\text{N} + ^{103}\text{Rh}$ system up to 400 MeV. The present theoretical analysis was done by using the Hybrid Monte Carlo Simulation (HMS) model, using three different forms of the nuclear level density, namely, Obninsk (OB), Kataria-Ramamurthy (KR) and back-shifted Fermi-Gas (FG). We have corrected an error in ALICE2014 which was leading to incorrect results for KR level-densities. In the HMS model the decay of the composite system is initially followed in terms of nucleon-nucleon collisions. Unlike previous versions, there are no adjustable parameters in ALICE2014 for this phase of the reaction. After the system cools sufficiently, the usual statistical model is applied and in this phase the nuclear level

density plays a crucial role in deciding the final population of residues. At each step of statistical decay, particle emission rates depend on the ratio of level densities of residual and parent systems.

The overall trends of the predicted excitation functions are satisfactory. The absolute values generally agree well with the experimental data for lighter isotopes and at energies above 200 MeV, with the OB level density. The latter region is the one where pre-equilibrium emission of nucleons and light clusters dominates and is therefore a more important region for the test of the present pre-equilibrium model. Considering the various options for the level densities, it was observed that the Kataria-Ramamurthy level densities lead to predictions very far from the data. In general it may be concluded that the calculations with HMS model (ALICE 2014) with OB level densities has qualitative trends similar to the data and reasonable quantitative agreement at the higher energies. The OB level density gives a fairly good description of the excitation functions for the observed isotopes of Cd, Ag, Pd, Rh, Ru and Tc, in that the general features are reproduced. The new code ALICE2014, which incorporates pre-equilibrium multi-nucleon and cluster emission in addition to the emission of single nucleons, satisfactorily describes the underlying mechanism for the production of heavy residues induced by medium-mass ions at intermediate energies. In general, it may also be concluded that the present experimental and theoretical calculations are in close agreement with those obtained earlier for $^{12}\text{C}+^{103}\text{Rh}$ system.

ACKNOWLEDGEMENTS

One of the authors (GFS) thanks RSICC, ORNL, USA for providing the ALICE2014 code for present theoretical analysis.

REFERENCES

1. M. Cavinato, E. Fabrici, E. Gadioli, E. Gadioli Erba, P.Vergani, M. Crippa, G. Colombo, I. Redaelli, and M. Ripamonti, *Phys. Rev. C* **52**, 2577 (1995).
2. E.Z. Buthelezi, F. Cerutti, E. Gadioli, G.F. Steyn, S.H. Connell, and A.A. Cowley, *Nucl. Phys. A* **753**, 29 (2005).

3. E.Z. Buthelezi, F. Cerutti, E. Gadioli, G.F. Steyn, A. Pepe, S.H. Connell, and A.A. Cowley, *Eur. Phys. A* **28**, 193 (2006).
4. M.B. Chadwick, P.G. Young, S. Chiba, S.C. Frankle, G.M. Hale, H.G. Hughes, A.J. Koning, R.C. Little, R.E. MacFarlane, R.E. Prael, and L.S. Waters, *Nucl. Sci. Eng.* **131**, 293 (1999).
5. P. Vergani, E. Gadioli, E. Vaciago, E. Fabrici, E. Gadioli Erba, M. Galmarini, G. Ciavola, and C. Marchetta, *Phys. Rev. C* **48**, 1815 (1993).
6. E. Gadioli, C. Birattari, M. Cavinato, E. Fabrici, E. Gadioli Erba, V. Allori, F. Cerutti, A. Di Filippo, S. Vailati, T.G. Stevens, S.H. Connell, J.P.F. Sellschop, F.M. Nortier, G.F. Steyn, and C. Marchetta, *Nucl. Phys. A* **641**, 271 (1998).
7. E. Gadioli, M. Cavinato, E. Fabrici, E. Gadioli Erba, C. Birattari, I. Mica, S. Solia, G.F. Steyn, S.V. Förtsch, J.J. Lawrie, F.M. Nortier, T.G. Stevens, S.H. Connell, J.P.F. Sellschop, and A.A. Cowley, *Nucl. Phys. A* **654**, 523 (1999).
8. C. Birattari, M. Bonardi, M. Cavinato, E. Fabrici, E. Gadioli, E. Gadioli Erba, F. Groppi, M. Bello, C. Bovati, A. Di Filippo, T.G. Stevens, S.H. Connell, J.P.F. Sellschop, S. J. Mills, F.M. Nortier, G.F. Steyn, and C. Marchetta, *Phys. Rev. C* **54**, 3051 (1996).
9. M. Blann, *Nucl. Phys. A* **235**, 211 (1974).
10. M. Blann and H.K. Vonach, *Phys. Rev. C* **28**, 1475 (1983).
11. M. Blann, *Annu. Rev. Nucl. Sci.* **25**, 123 (1975).
12. M. Blann and M.B. Chadwick, *Phys. Rev. C* **57**, 233 (1998).
13. M.B. Chadwick and P. Obložinský, *Phys. Rev. C* **50**, 2490 (1994).
14. E. Gadioli, E. Gadioli-Erba and P.G. Sona, *Nucl. Phys. A* **217**, 589 (1973). E. Gadioli and E. Gadioli-Erba, *Nucl. Inst. Methods*, **146**, 265 (1977).
15. M. Blann, *Phys. Rev. Lett.* **28**, 757 (1972).
16. M. Blann and A.Y. Konobeev, Precompound Cluster Decay in HMSALICE (2008), Unpublished, Available in documentation supplied with RSICC Code Package PSR-550, <https://rsicc.ornl.gov/>.
17. M. Blann, *Phys. Rev. C* **54**, 1341 (1996).
18. S.G. Mashnik, K.K. Gudima, A.J. Sierk, M.I. Baznat, and N.V. Mokhov, CEM03.01 User Manual, LANL Report LA-UR-05-7321 (2005).

19. R.B. Firestone and V.S. Shirley (ed) *Table of Isotopes* 8th edition, (New York: Wiley) (1996); Firestone and Eckström, *WWWTable of Radioactive Isotopes*, Version 2.1 (2014), Available from <http://ie.lbl.gov/toi>.
20. V.F. Weisskopf and D.H. Ewing, *Phys. Rev.* **57**, 472 (1940).
21. S.K. Kataria, V.S. Ramamurthy, and S.S. Kapoor, *Phys. Rev. C* **18**, 549 (1978).
22. A.V.Ignatyuk, J.L.Weil, S.Raman, and S.Kahane, *Phys. Rev. C* **47**, 1504 (1993).

Table I. Measured cross sections of residues formed in the interaction of ^{14}N with ^{103}Rh up to 400 MeV.

Energy (MeV)	σ (mb)						
	^{103}Ag	^{104}Ag	^{105}Ag	^{104}Cd	^{99}Pd	^{100}Pd	^{101}Pd
89.4	--	--	12.8±1.4	--	--	9.32±1.2	8.0±2.3
110.9	--	--	122±13.4	20.3±4.0	--	24.7±3.2	27.5±5.3
129.7	--	--	228±27.4	32.3±4.3	--	55.9±8.4	45.8±6.8
146.7	15.6±3.2	20.7±1.2	223±24.5	30.3±4.1	6.13±0.78	87.6±12.9	71.8±8.5
162.3	44.8±8.9	103±7.3	331±36.5	45.4±4.5	8.13±1.14	135±18.9	143±11.9
176.8	55.3±10.5	146±11.8	389±38.6	64.2±6.6	9.06±1.26	166±21.6	190±13.8
190.5	83.2±15.8	130±9.1	310±34.1	105±13.8	26.5±2.9	234±28.5	204±14.3
203.5	102±8.6	132±6.2	241±28.9	110±14.3	33.4±4.0	256±31.7	218±14.8
215.8	96.1±10.8	116±4.6	203±24.6	137±13.8	41.2±4.7	293±35.2	221±14.8
227.7	94.8±5.7	91.5±3.3	170±19.7	117±14.8	32.3±3.8	287±34.4	230±15.2
239.0	124±4.3	87.8±3.3	146±12.8	120±15.2	40.5±5.2	326±35.9	228±15.1
250.0	134±9.8	77.5±3.6	114±10.9	114±15.1	53.4±7.0	171±25.6	184±13.6
250.9	145±9.6	56.5±2.4	111±10.2	104±13.6	52.8±7.2	131±18.3	202±14.2
261.7	133±15.9	49.1±2.2	116±10.8	107±14.2	50.5±6.5	190±22.8	195±13.9
271.9	84.1±5.0	28.2±2.8	126±11.3	114±13.9	44.5±6.0	112±16.8	141±11.9
281.8	63.0±11.4	20.0±1.0	49.8±5.4	97.8±10.9	45.7±5.5	188±22.6	164±12.8
291.5	71.9±15.4	19.3±1.6	61.4±5.5	61.7±8.1	38.9±5.5	129±19.4	145±12.0
300.9	57.3±15.3	17.1±1.7	52.7±5.1	50.9±7.0	45.4±6.7	179±23.3	141±11.9
310.1	50.7±11.6	16.2±1.6	31.4±3.2	40.8±5.2	36.4±4.9	115±16.1	124±11.1
319.1	45.0±13.5	12.6±1.5	27.6±3.6	32.4±4.6	38.4±5.4	91.3±13.9	142±11.9
327.9	39.1±8.3	9.9±1.3	32.1±3.8	30.9±4.4	28.5±4.4	152±25.9	142±11.9
336.5	38.8±8.2	9.9±0.8	23.6±3.0	35.3±6.2	27.6±3.6	156±26.5	129±11.4
344.9	31.9±7.0	9.3±1.4	25.2±3.1	26.9±5.8	23.5±3.6	123±20.9	121±11.0
353.2	34.0±7.1	7.7±1.1	23.1±2.7	28.7±7.0	24.0±3.8	153±30.6	113±10.6
361.4	25.0±5.7	6.4±0.8	31.2±3.4	29.2±5.9	23.4±3.9	121±19.4	129±11.3
369.3	28.4±6.1	6.9±1.0	32.2±3.3	22.1±4.9	17.6±3.4	133±23.9	107±10.3
377.2	20.8±9.6	6.3±0.7	23.9±2.9	22.6±4.5	--	107±19.2	109±10.4
384.9	21.1±5.0	6.7±1.5	17.9±2.0	22.5±4.5	--	118±22.4	94.0±9.7
392.5	22.1±5.1	7.9±1.3	24.7±2.9	19.3±3.7	--	150±28.5	95.8±9.8
400.0	20.7±4.2	6.4±1.2	11.5±2.1	18.8±3.8	--	--	--

Table II. Measured cross sections of residues formed in the interaction of ^{14}N with ^{103}Rh up to 400 MeV (continued).

Energy MeV	σ (mb)							
	^{97}Rh	^{99}Rh	^{101}Rh	^{95}Ru	^{97}Ru	^{94}Tc	^{95}Tc	^{96}Tc
89.4	--	--	--	--	--	--	--	--
110.9	--	--	35.1±4.2	--	--	--	--	--
129.7	--	--	80.2±9.6	--	--	--	--	--
146.7	--	11.0±1.5	113±15.8	--	20.7±2.7	--	--	--
162.3	--	39.5±4.8	149±19.4	--	18.5±2.4	3.7±0.6	2.7±0.05	--
176.8	--	60.7±9.5	252±35.1	--	34.2±5.5	5.0±0.8	6.5±0.1	--
190.5	9.9±1.2	78.7±11.4	314±33.6	14.5±2.0	63.7±8.9	7.1±1.3	13.2±0.3	13.3±2.4
203.5	20.6±2.3	94.7±12.3	388±46.6	16.4±2.8	82.4±12.3	11.2±2.1	23.9±0.6	19.1±3.1
215.8	19.4±2.5	148±13.7	348±38.3	20.6±3.9	105±13.9	16.8±3.5	34.1±0.8	23.3±5.3
227.7	23.4±3.2	162±15.4	351±45.6	22.0±3.8	147±14.7	17.4±5.4	51.5±1.3	30.2±4.2
239.0	37.5±4.8	171±18.9	375±41.3	41.0±7.0	150±16.5	21.6±7.1	73.9±1.9	35.0±4.1
250.0	36.6±4.7	165±15.3	357±42.8	39.3±6.1	182±20.0	17.7±4.4	96.6±2.5	36.8±2.1
250.9	29.4±3.5	146±19.7	311±33.5	31.2±5.1	131±20.9	16.3±3.3	117±2.7	32.2±6.1
261.7	41.7±5.7	170±23.1	329±46.1	45.9±5.7	154±18.6	22.6±4.1	68.9±1.6	34.3±6.5
271.9	48.6±6.7	254±27.9	314±33.9	56.5±7.0	228±31.9	30.7±7.4	98.5±2.4	40.9±8.6
281.8	37.4±5.5	188±21.7	313±34.4	57.5±7.9	191±28.7	30.4±3.9	111±2.8	37.1±6.3
291.5	58.7±8.7	187±26.2	348±31.3	53.2±7.5	252±45.4	38.7±8.4	100±2.6	43.3±8.2
300.9	52.5±9.3	167±23.4	330±33.0	56.8±7.9	224±42.5	44.6±7.5	134±4.3	39.5±7.1
310.1	60.2±11	171±25.6	303±33.3	61.5±8.0	247±29.6	49.1±6.9	141±4.1	42.4±6.4
319.1	48.9±5.8	149±14.6	281±33.7	65.2±8.4	208±33.3	71.3±11.1	150±4.0	43.2±8.5
327.9	50.2±8.0	150±17.9	263±34.2	63.0±9.5	235±28.2	70.7±9.9	157±5.9	53.6±8.5
336.5	53.1±7.4	175±24.5	283±33.9	68.4±9.6	242±26.6	59.7±4.9	152±5.7	45.5±5.0
344.9	52.0±11	153±19.9	264±42.2	75.9±12.1	255±33.2	79.7±10.9	173±4.2	53.0±4.0
353.2	53.7±11	150±24.2	267±37.4	78.5±10.2	236±40.1	68.3±8.8	182±5.7	59.0±3.6
361.4	45.7±5.5	165±23.1	233±34.9	76.1±16.0	241±43.4	70.5±6.8	183±5.8	46.5±1.6
369.3	46.6±12	129±21.9	244±39.0	81.7±13.8	229±43.5	91.7±10.8	168±3.4	55.2±2.7
377.2	41.6±3.8	130±22.8	201±33.6	79.9±15.2	210±37.8	86.3±6.1	187±6.4	49.2±9.2
384.9	44.6±15	139±24.7	216±32.1	78.1±17.9	188±37.6	79.1±10.5	160±5.1	58.4±2.5
392.5	40.1±8.3	142±26.9	209±29.3	83.4±18.3	205±45.1	59.8±8.0	165±5.1	61.4±2.4
400.0	41.6±5.4	107±17.1	124±14.9	75.8±15.9	169±32.1	56.7±8.5	162±4.8	56.2±1.8

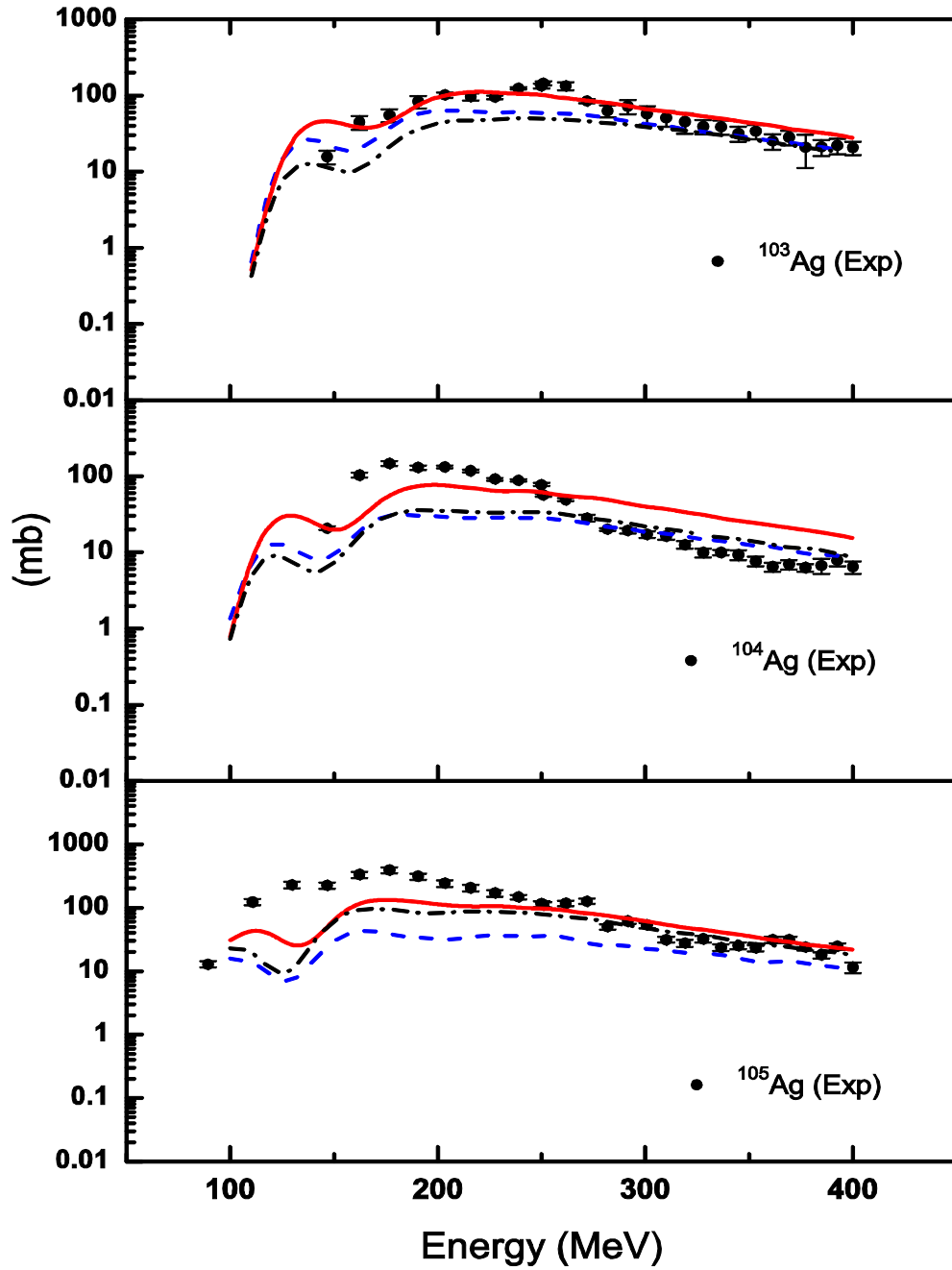


FIG. 1. (Color online) Excitation functions of Ag residues formed in the interaction of ^{14}N with ^{103}Rh , as indicated. The solid symbols are the experimental results of this work. The calculated excitation functions are shown as red solid curves (OB level density) and blue dash curve (FG level density) and black dash-dot curves (KR level density) as obtained with the nuclear reaction code ALICE 2014.

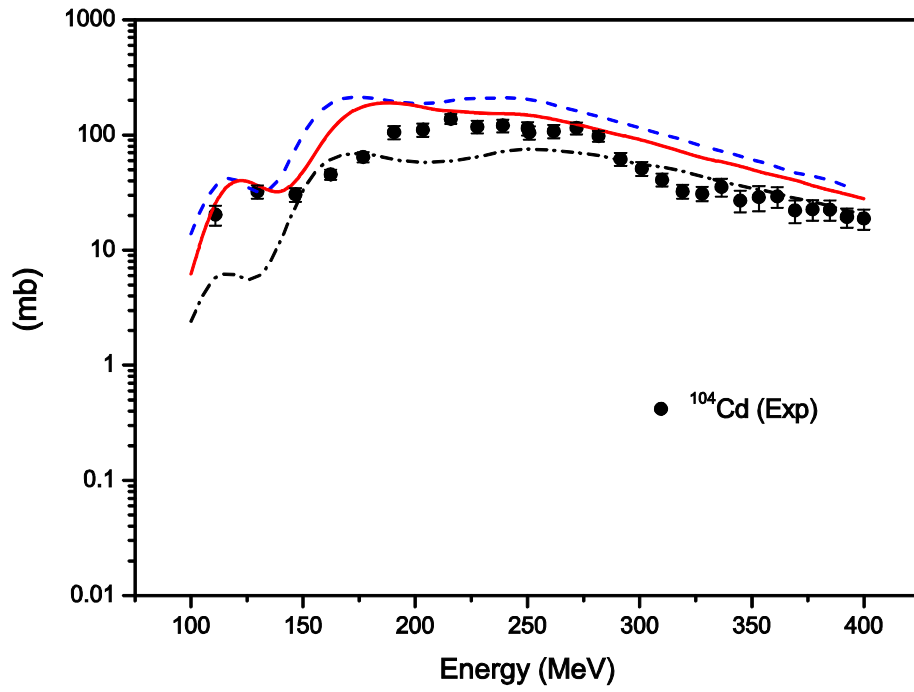


FIG. 2. (Color online) Excitation function of ^{104}Cd residues formed in the interaction of ^{14}N with ^{103}Rh . Also see caption to FIG. 1 for more detail.

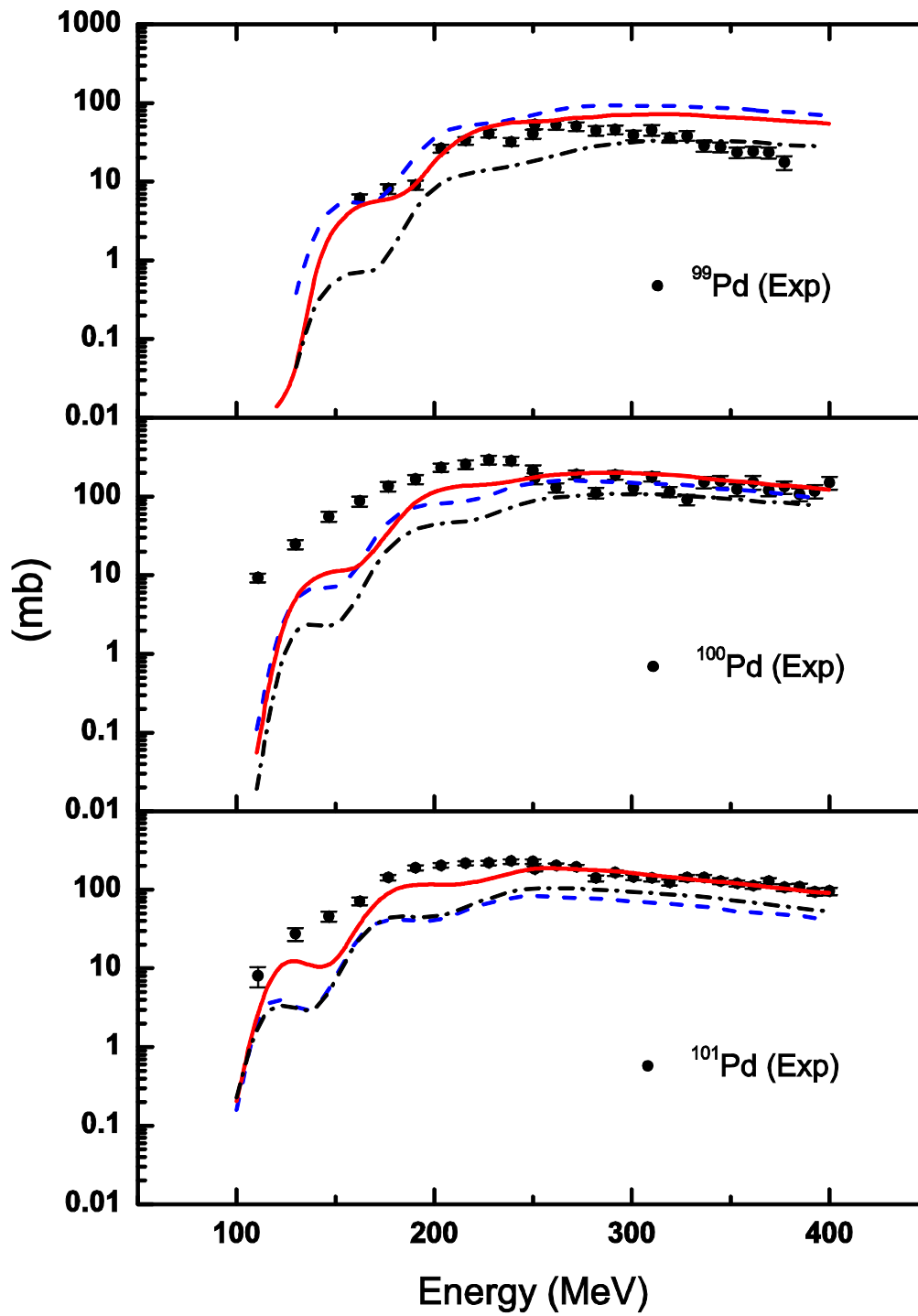


FIG. 3. (Color online) Excitation functions of Pd residues formed in the interaction of ^{14}N with ^{103}Rh , as indicated. Also see caption to FIG. 1 for more detail.

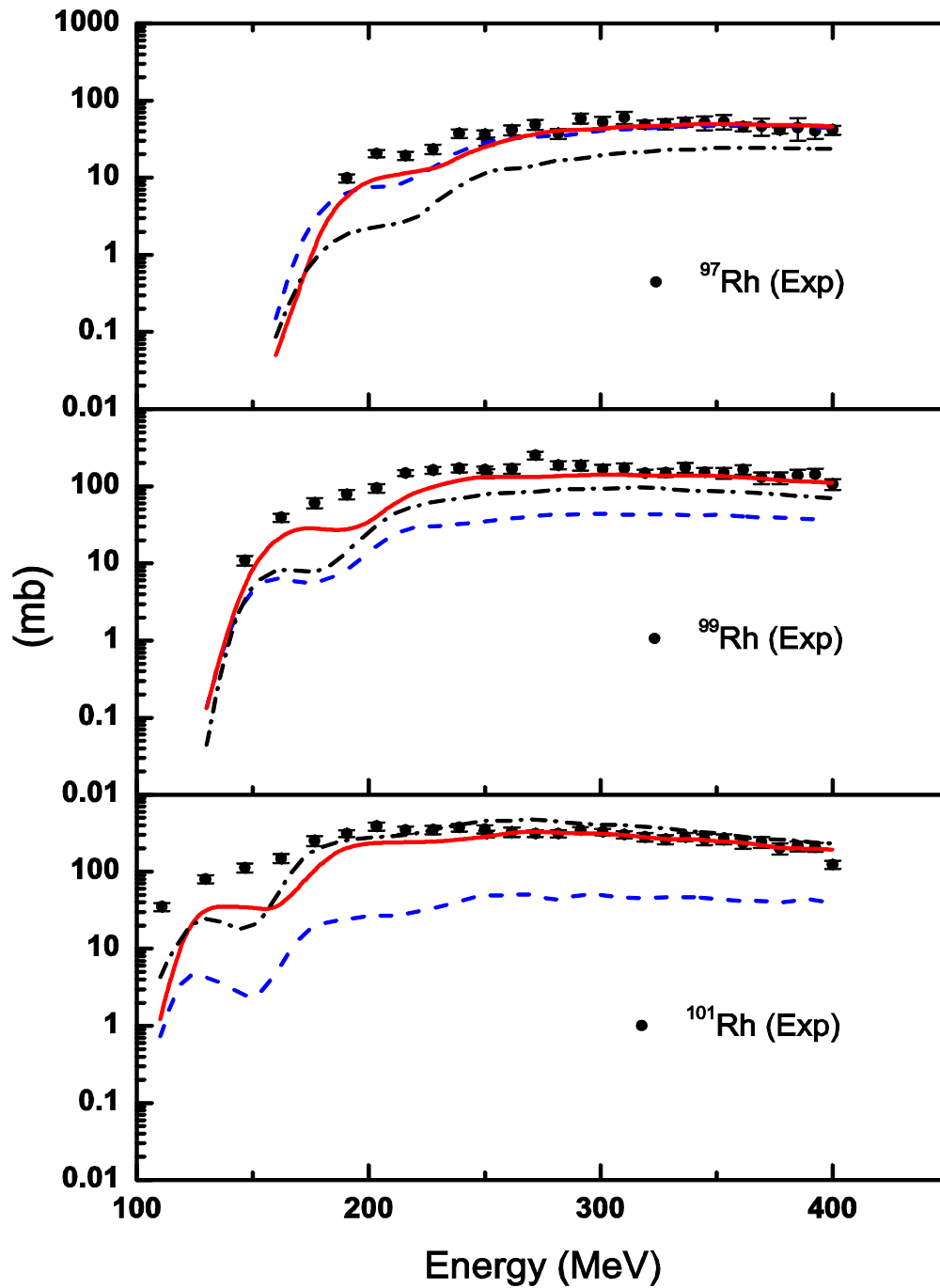


FIG. 4. (Color online) Excitation functions of Rh residues formed in the interaction of ^{14}N with ^{103}Rh , as indicated. Also see caption to FIG. 1 for more detail.

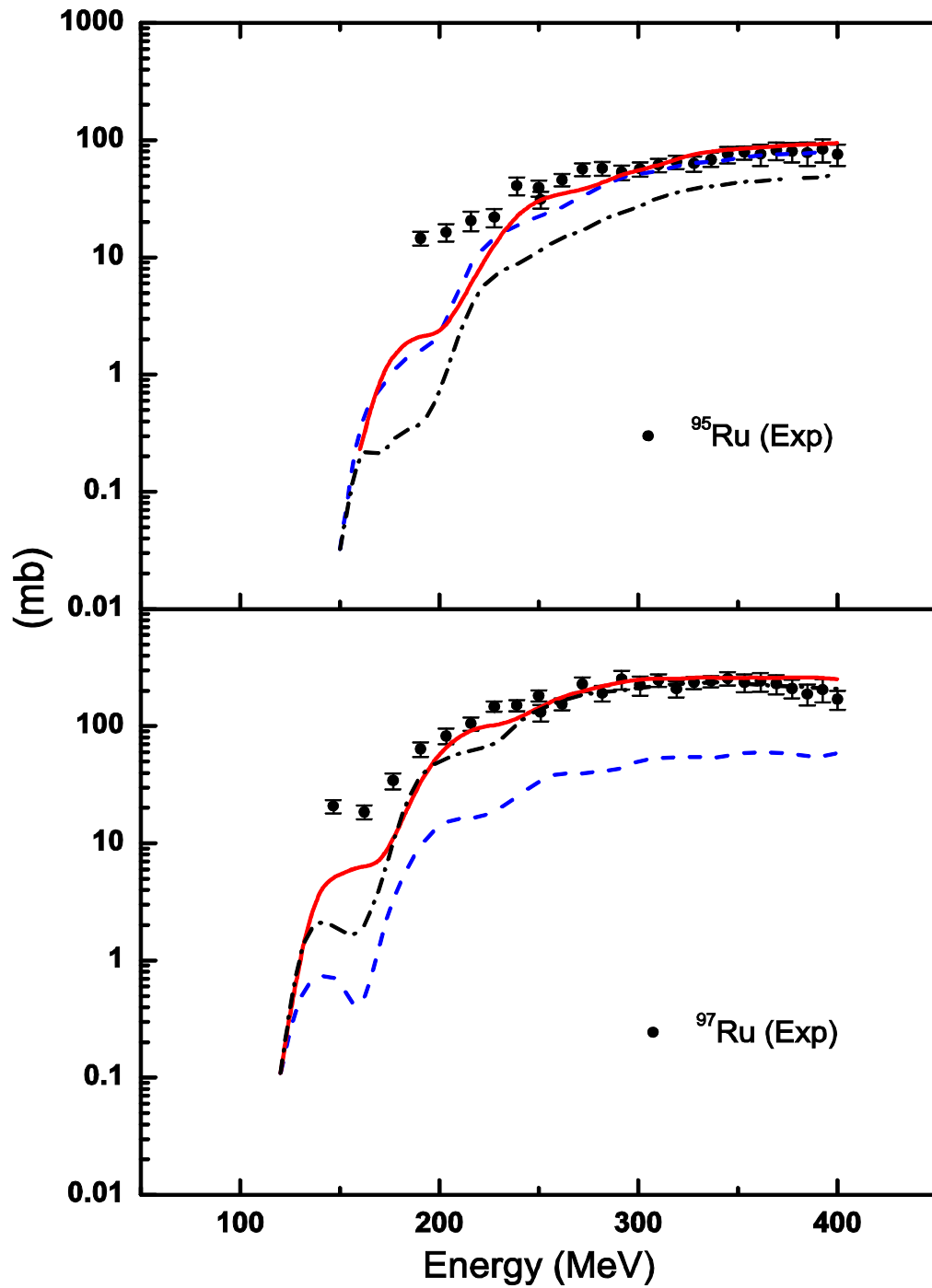


FIG. 5. (Color online) Excitation functions of Ru residues formed in the interaction of ^{14}N with ^{103}Rh , as indicated. Also see caption to FIG. 1 for more detail.

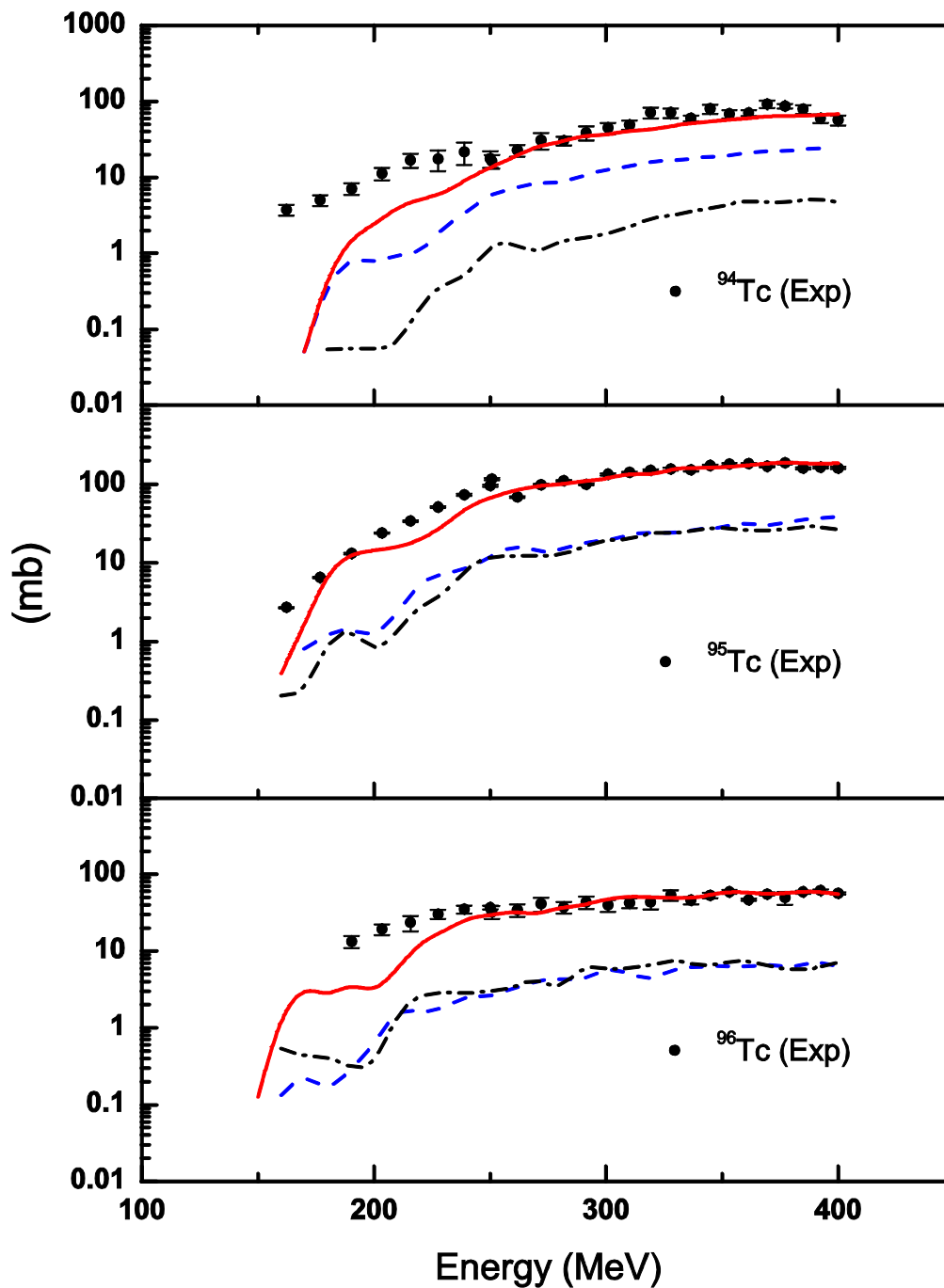


FIG. 6. (Color online) Excitation functions of Tc residues formed in the interaction of ^{14}N with ^{103}Rh , as indicated. Also see caption to FIG. 1 for more detail.

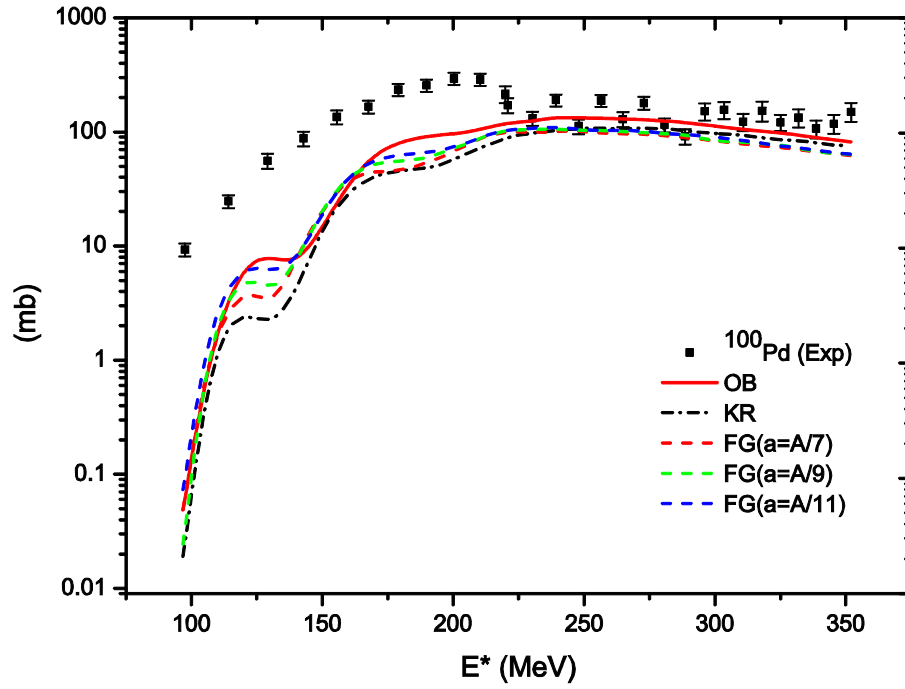


Fig. 7. (Color online) Excitation function ^{100}Pd residue in the $^{14}\text{N}+^{103}\text{Rh}$ reaction with different level density options.

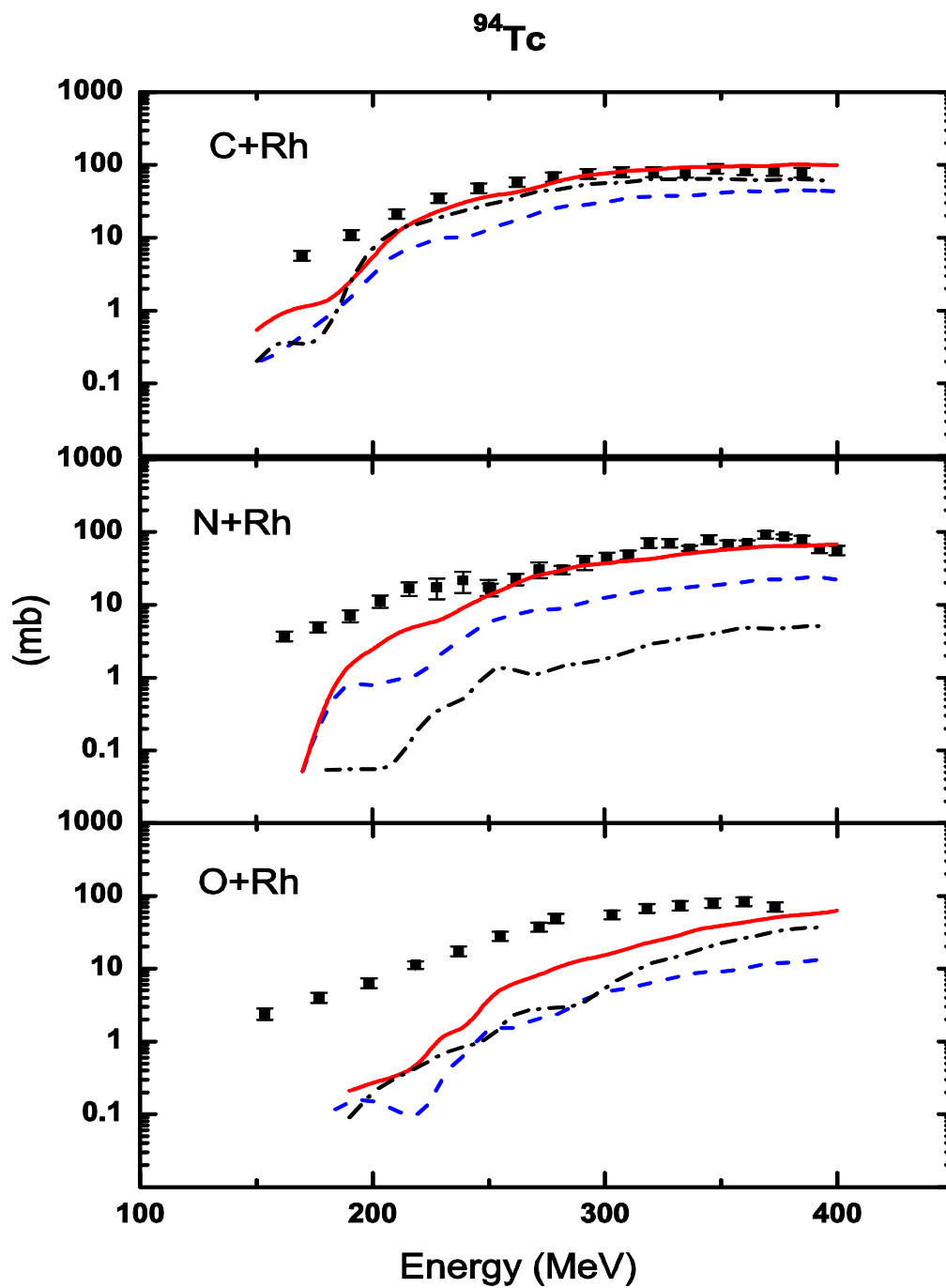


Fig. 8. (Color online) Inter comparison of excitation functions of ^{94}Tc for ^{12}C , ^{14}N , ^{16}O + ^{103}Rh systems. Theoretical calculations with HMS model are shown by Solid red curve (OB), dashed blue curve (FG) and black dash-dot curve (KR).

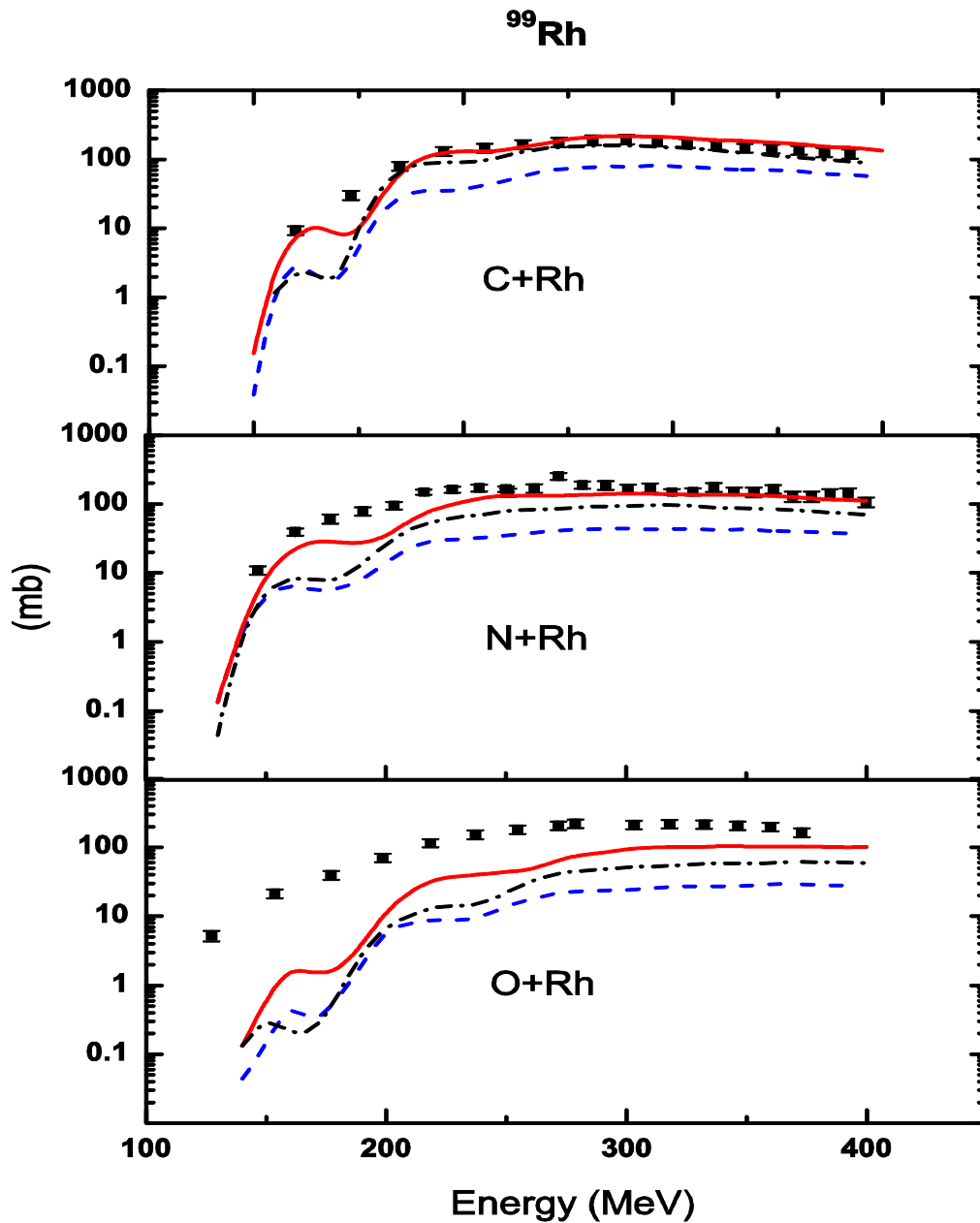


Fig. 9. (Color online) Inter comparison of excitation functions of ^{99}Rh for ^{12}C , ^{14}N , ^{16}O + ^{103}Rh systems. Theoretical calculations with HMS model are shown by Solid red curve (OB), dashed blue curve (FG) and black dash-dot curve (KR).

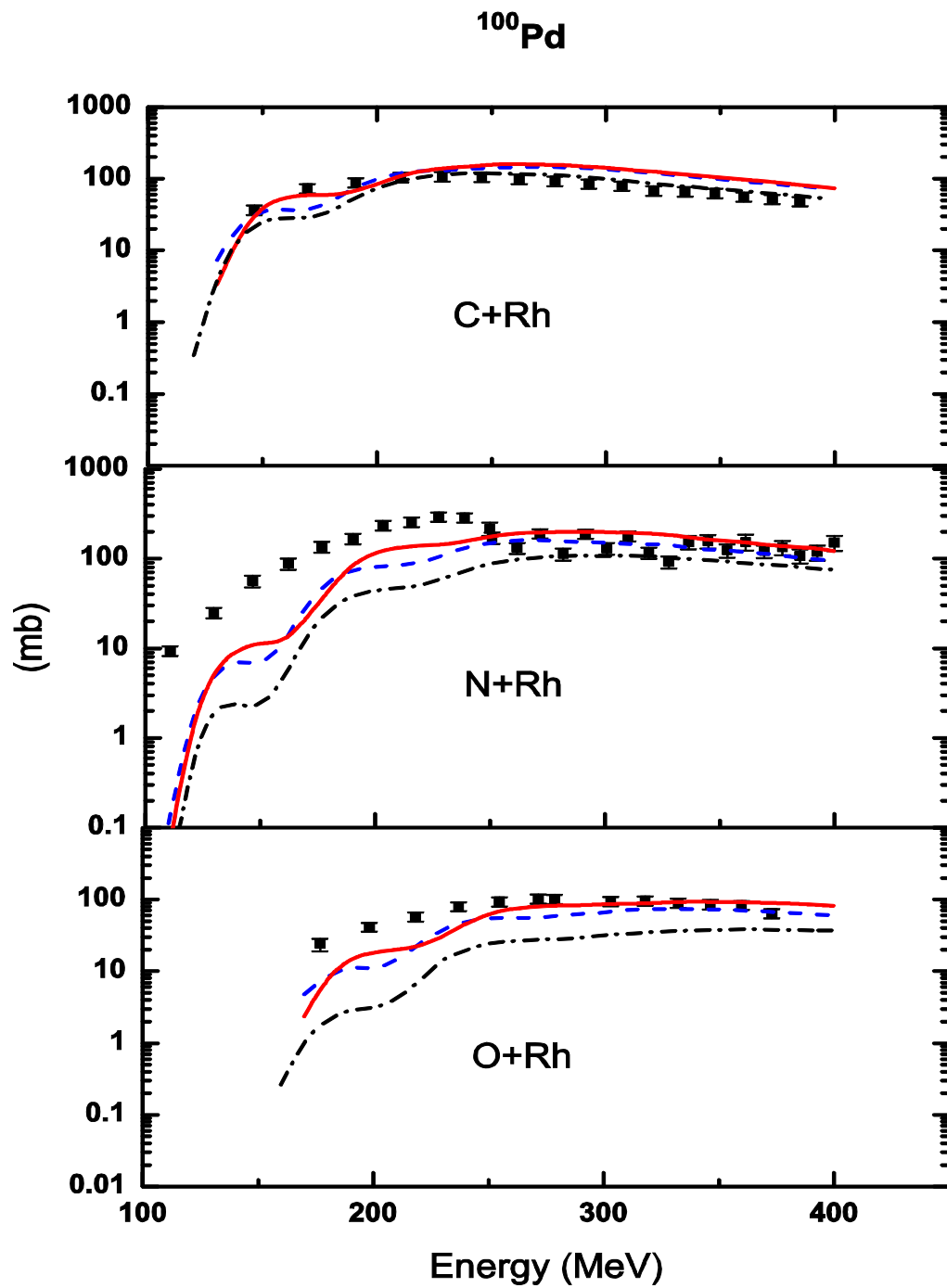


Fig. 10. (Color online) Inter comparison of excitation functions of ^{100}Pd for ^{12}C , ^{14}N , ^{16}O + ^{103}Rh systems. Theoretical calculations with HMS model are shown by Solid red curve (OB), dashed blue curve (FG) and black dash-dot curve (KR).

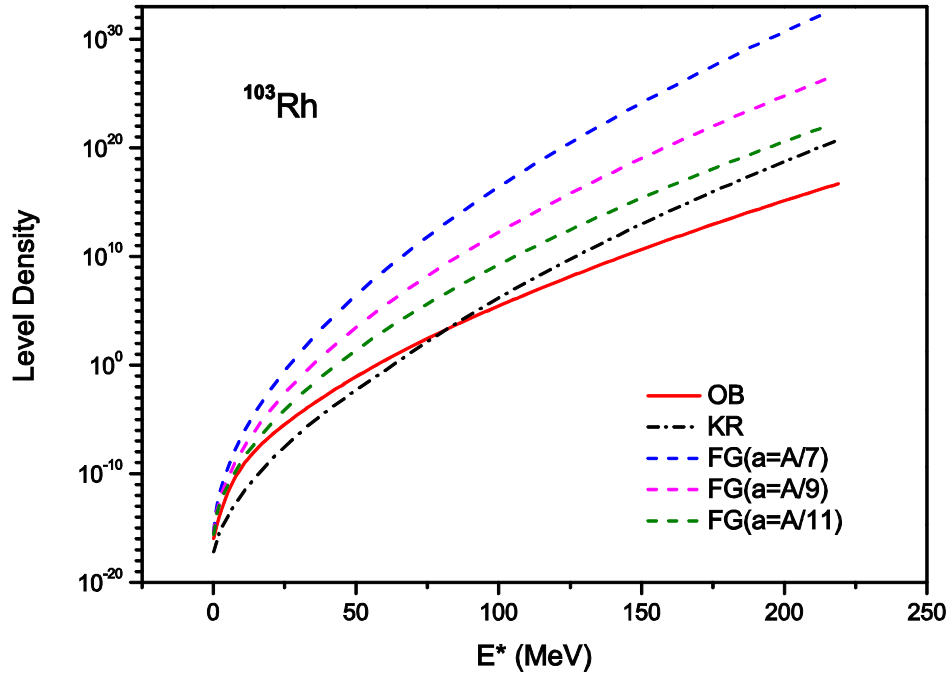


Fig. 11. (Color online) Level density of ^{103}Rh isotope as a function of excitation energy for $\square = 0$, for different options as indicated.